Microporosity and nanostructure of activated carbons: characterization by X-ray diffraction and scattering, Raman spectroscopy and transmission electron microscopy

Andrei A Shiryaev, Pascaline Pré, Cédric Pardanaud, Vadim Murzin, Alexei Averin, Jean-Noël Rouzaud

▶ **To cite this version:**

Andrei A Shiryaev, Pascaline Pré, Cédric Pardanaud, Vadim Murzin, Alexei Averin, et al.. Microporosity and nanostructure of activated carbons: characterization by X-ray diffraction and scattering, Raman spectroscopy and transmission electron microscopy. Adsorption - Journal of the International Adsorption Society, 2023, 10.1007/s10450-023-00406-x . hal-04172745

HAL Id: hal-04172745
https://hal.science/hal-04172745v1

Submitted on 28 Jul 2023

HAL is a multi-disciplinary open access archive for the deposit and dissemination of scientific research documents, whether they are published or not. The documents may come from teaching and research institutions in France or abroad, or from public or private research centers.

L'archive ouverte pluridisciplinaire **HAL**, est destinée au dépôt et à la diffusion de documents scientifiques de niveau recherche, publiés ou non, émanant des établissements d'enseignement et de recherche français ou étrangers, des laboratoires publics ou privés.

Microporosity and nanostructure of activated carbons: characterization by X-ray diffraction and scattering, Raman spectroscopy and Transmission Electron Microscopy

Andrei A. Shiryaev[1*], Pascaline Pré[2], Cédric Pardanaud[3], Vadim Murzin[4], Alexei Averin[1], Jean-Noël Rouzaud[5]

[1] A.N. Frumkin Institute of Physical Chemistry and Electrochemistry of Russian Academy of Sciences, Leninsky pr. 31, korp. 4, Moscow 119071, Russia

[2] Laboratoire de GÉnie des Procédés – Agroalimentaire – Environnement (GEPEA), UMR CNRS 6144, Mines de Nantes, Nantes, France

[3] PIIM, UMR CNRS 7345, Université Aix-Marseille, Avenue Escadrille Normandie-Niémen, 13397 Marseille Cedex 20, France

[4] EFFECT Photonics B.V., Kastanjelaan 400, 5616 LZ Eindhoven, The Netherlands

[5]Laboratoire de Géologie, Ecole Normale Supérieure, UMR CNRS 8538, 75231 Paris, France

* Corresponding author (email: shiryaev@phyche.ac.ru)

Abstract.

Microporosity and structure of a set of activated carbons was studied by combination of N_2 and CO_2 adsorption, Transmission Electron Microscopy (TEM), X-ray diffraction and scattering and multiwavelength Raman spectroscopy. It is shown that correlations between measured parameteres may be established for a given set of activated carbons, most often obtained from a same precursor. Comparison of results of TEM images processing and of Small-angle scattering with adsorption data suggests that super-micropores (0.7-2 nm) are highly variable in shape and strongly deviate from the ideal slit pore model. These pores are likely located in between disordered continuous graphene stacks. It is shown that Small-angle scattering is mostly caused by supermicropores; contribution of other types of porosity is of secondary importance. For a set of carbons with similar structure, a reasonable correlation between Guinier radii and pore width obtained from N_2 adsorption can be found; however, the reason for the observed offset between the data sets remain uncertain. Sensitivity of the Raman scattering to atomic scale processes leads to poor or unclear correlations between the spectroscopic and structural data, although some notable exceptions are noted.

Keywords: Activated carbon; structure; TEM; SAXS; Raman; adsorption

1. Introduction

The sorption capacity and efficiency of carbon adsorbents largely depend on pore size distribution and on structure of a pore-matrix interface. Analysis of vapour adsorption isotherms is a well established important method of investigation of the porous structure. The effective pore size is usually calculated in the framework of Dubinin's volume filling theory (MVFT) (Dubinin 1975, Dubinin 1989), density functional theory (DFT) (Ustinov and Do, 2004), Kawazoe or BJH equations (Gregg and Sing, 1982). Most activated carbons (ACs) are composed of cross-linked highly defective graphene sheets arranged in stacks of various sizes and thicknesses, designated as basic structural units (BSUs). Understanding of structure of the stacks and of their mutual arrangement remains a highly challenging task due to general lack of long-range ordering and necessity to investigate the system at different scales. High Resolution TEM (HRTEM) permits direct imaging of the carbon skeleton after appropriate image analysis, however, information about the pores is more elusive. A dedicated approach based on visualization of edges of graphene sheets allowed characterization of a large set of activated carbons (Pre et al., 2013). Statistical data representative of the fringe geometry (length, tortuosity and curvature radii) were extracted together with data on their spatial arrangement. Whereas this method gives unprecedented information at atomic scale, a well-known disadvantage of HRTEM is the problem of how representative are selected images if one intends to describe the entire sample. Approaches comprising detailed TEM investigation complemented by advanced modeling (Leyssalle et al., 2012) are very promising, but at present, the number of studied materials is still rather limited due to significant efforts required for every individual sample. Structural information on the nanometer is also provided by X-ray diffraction (XRD) and Small angle scattering (SAXS); Raman spectroscopy provides some data on atomic vibrations and arrangement. The latter methods are nondestructive and rather fast compared to sorption and TEM experiments but average information from a large volume (hundreds – thousands μm^3) and extracted structural parameters differ from those obtained from TEM. The only reliable way to investigate the sorbent structure in detail is the application of several complementary techniques to the same set of samples.

In this work we present results of investigation of a set of activated carbons (ACs) prepared from very different precursors. Several complementary analytical methods were employed to assess structure and properties of the samples: N_2 and CO_2 adsorption, X-ray Small-angle scattering (SAXS) and diffraction using conventional laboratory source and high-energy radiation, multi-wavelength Raman spectroscopy and HRTEM with image processing.

The information about structure of a set of ACs from different precursors on different scales is summarized and compared with adsorption data. The analytical methods provide information about various structural scales and are not necessarily well correlated. Raman spectroscopy gives information about structure and defects in graphene sheets and stacks at the smallest, almost atomic scale. X-ray diffraction is more sensitive to ordered material. SAXS provides information about nanometer-scale heterogeneities, giving some insights into porous structure, responsible for adsorption. Finally, TEM bridges information from several spatial levels.

2. MATERIALS AND METHODS

2.1. Samples

The set of the studied adsorbents includes both commercial and non-commercial activated carbons produced from different precursors (Table 1). With the exception of the adsorption methods, all samples were studied in as-received state.

Activated carbons made from furfural (FAS-type) were developed at SPA "Neorganika" (Electrostal, Russia). Extreme mechanical strength of these materials and high sorption capacity of this type of AC make them extremely important in applications requiring high mechanical and adsorption properties, e.g., biomedicine, radiochemistry etc. (Tsivadze et al., 2011). The general production scheme of the FAS-type ACs' is the following: 1) liquid moulding of synthetic furfural monomer at 105 ºC, 2) carbonization of spheroidal sorbent grains in inert medium at 750 ºC, 3) steam activation at 850 ºC. The samples differ by duration of the activation process lasting from 5 to 15 hours. After the activation, the spheroidal grains are washed in distilled water and dried.

The MUST samples were made at GEPEA (Nantes, France) from pine wood by steam activation at low temperatures, indicated in the sample name (e.g., MUST-750, etc). The other studied materials are represented by commercial activated carbons. Similar to the MUST samples, the BGX was also made from pine wood, but mixed physical and chemical activation was employed. The BPL and NC materials were produced by physical activation from bituminous coal and coconut shell, respectively. The TMC was also made from bituminous coal; after the activation it was submitted to hydrocarbon deposition treatment to reduce the micropore opening. For this reason, micropores in TMC are accessible for CO_2, but not for N_2 at 77 K; thus the sample resembles carbon molecular sieve. The GF40 sample was made by chemical (phosphoric acid) activation of olive seeds.

2.2. Characterisation

The measurements of ultra-micropore volume were performed using CO_2 adsorption isotherms at 273 K; the calculations were performed using Dubinin-Radushkevich equation (Dubinin 1968). Supermicropores were studied using N_2 adsorption at 77 K; their volume was evaluated using α_S (Atkinson et al., 1984) and NLDFT (Jagiello & Olivier, 2009) methods.

High Resolution Transmission Electron Microscopy (TEM) images were acquired on a Tecnai F20 ST (FEI) operating at 200 kV and equipped with a Field Emission Gun. The samples were dispersed in ethanol by ultrasonic agitation and dropped onto a lacey carbon grid. The 002 lattice fringe mode with magnification of up to 500000×, was used to image profiles of the aromatic layers. The image processing algorithm used in this study is based on morphological modeling. Details about the HRTEM image processing method can be found in (Pre et al., 2013).

Small- and Wide Angle X-ray scattering (SWAXS) patterns were recorded using monochromatic CuKα-radiation in a broad range of scattering vectors ($q=4\pi\sin\Theta/\lambda$) spanning range from 0.1–27 nm^{-1} using dedicated diffractometer SAXSess (Anton Paar GmbH). A Kratky block collimation scheme was employed (Kratky, 1982). Since the measurements were performed in slit geometry, desmearing was performed using SAXS Suite software (Anton Paar GmbH) employing approach developed by Lake (1967). The samples were measured in standard X-ray capillaries or between two layers of special polymer film. All measurements were performed at room temperature in evacuated chamber at a residual pressure of 5–10 mbar. Due to high brightness of the setup, the total exposure of the samples to vacuum was less than 5 minutes. Eventual water losses upon air pumping and other relevant issues, which might influence the SAXS measurements, were controlled using several modes of vacuum annealing. No changes in the scattering patterns were observed (Shiryaev et al., 2017). Prior to the data evaluation, the scattering from the holder was subtracted and the scattering patterns were normalized to X-ray absorption of the sample. Further details of the data analysis are given in the corresponding part of the manuscript.

X-ray diffraction patterns were recorded using Empyrean (Panalytical BV) diffractometer in Bragg–Brentano geometry using Ni-filtered CuKα-radiation in the angular range 10–120º (2Θ). No binder was employed to exclude eventual influence on sorbent structure (Vartapetyan and Khozina, 2006). All reported patterns were acquired for the samples dried directly on the X-ray holder in hot air for several hours, see below for detail.

High energy XRD measurements were made on several representative samples sealed in 1.5 mm glass capillaries at P02 beamline at PETRA III synchrotron source. Data treatment was performed using homemade software performing correction for incoherent and multiple scattering contributions, polarization, absorption, etc.

Raman spectra were acquired with Bruker Senterra microspectrometer in a quasi-backscattering geometry in air at room temperature using 532 and 785 nm lasers. Low laser power was employed and absence of the sample alteration by the beam was checked both visually and by controlling lack of changes in spectral features between repeated scans. Several scans were averaged to improve signal to noise ratio; in addition, at least two spots were analysed for every sample to assure consistency. Spectral decomposition to individual components is described in the corresponding part of the paper.

3. RESULTS AND DISCUSSION

3.1. Adsorption

For convenience, the studied samples are ranked according to the relative fraction of the supermicropores (0.7-2 nm) inferred from the CO_2 and N_2 adsorption data (Fig. 1). Volume of the supermicropores was estimated using both the α_S (Atkinson et al., 1984) and NLDFT (Jagiello & Olivier, 2009) methods. Despite significant scatter in the pore shapes, both methods give consistent results (Fig. 1). The supermicropores can be formed by discontinuities between stacked graphene sheets (for instance, caused by defects such as dislocations), and are located between or at the edges of the ordered structural units. As shown in (Pre et al., 2013), the slit shape pore model approximates reasonably well the actual morphology of the ultramicropores, which are formed by interstices between non-smooth (corrugated) graphene walls. The micropore size distribution was estimated using the HK model. Presumably, the largest pores should be located in the voids created by the random arrangement of the continuous domains. These results are discussed together with the TEM data in the following sections of the paper.

3.2. Nanostructural disorder and pore size distributions as inferred from Transmission Electron Microscopy

Typical TEM images and the processing results for representative samples are shown in Figs. 2 and 3. The employed method of TEM image processing (Pre et al., 2013) provides quantitative description of the spatial arrangement of the defective graphene fragments

comprising the carbon skeleton and enables to extract different properties of various types of the graphene ensembles. The following parameters were measured for the corresponding cases:

1) For each stack in the ensembles comprising several fringes: length $\bar{L}$, tortuosity $\bar{\tau}$, and the local curvature radii $\bar{R}_c$.
2) For the ensembles composed of nearly parallel fringe fragments, i.e. stacks or Bulk Structural Units (BSU): length $\bar{L}_{//}$ and the surface density $\%_{//}$ they cover over the whole set of fringes.
3) For the ensembles composed of the "continuous domains" defined as interconnected multi-layer stacks with a common orientation: the length of the fringes included in the domains $\bar{L}_d$, their surface density (relative to all fringes) $\%_d$, their size (perimeter $\bar{P}_d$ and surface area $\bar{A}_d$).

The degree of disorder of the AC nanostructure could be quantified based on the size and the surface density of the continuous domains. According to the TEM images analysis, the studied samples fall into two main groups: with high and moderate/low degrees of the disorder. These two groups are characterised by marked variations of sizes of the graphitic domains (Fig. 3) and differ in distribution of the fringe lengths (Fig. 2d), mean curvature radius and surface area of BSUs. However, parameters such as tortuosity, %BSU, $\bar{P}_d$, do not follow this simple classification. Namely, the samples SC, TMC and BGX form a special subgroup with markedly higher values of these parameters. The BGX and MUST carbons were both fabricated from a pine wood precursor, but BGX was submitted to mixed physical and chemical activation, whilst MUST underwent only low degree of physical activation. These materials present structural similarities: high surface densities of the stacks and continuous domains, resulting in large ordered assemblages. The values of the mean tortuosity and local curvature radius indicate a high fraction of nearly straight fringes, and, consequently, smaller amounts of point defects than in BPL, NC100 and FAS-type ACs. All these materials differ by their microporosity (Figs. 1, 2d). For the fufural-derived FAS samples, and BPL, NC-100 and GF40 ACs the fringe length in continuous domains is rather small (~0.5-0.6 nm), but total volume of ultra- and supermicropores varies in broad range. The other samples show smaller volume ($V_{ultra}+V_{super}$) and noticeably longer fringes, implying more ordered structure (Fig. 2d) The MUST specimen is mainly ultramicroporous and the pore size distribution evaluated from the adsorption data matches well the effective spaces

measured in the “all fringes” ensemble. In contrast, the BGX material contains a large fraction of supermicropores and in this case, the adsorption data correlate with the effective spaces measured in the domain ensemble (Fig. 4). The later situation corresponds to location of the supermicropores pores mainly between the stacked assemblages.

Figure 4 show distributions of the effective spaces extracted from the TEM images in the ensembles and the micropore size distributions derived from the HK model. The effective spaces ***w*** separating different structural entities are measured for each ensemble. For the entire range of the measured spaces - from 0 up to the maximum or restricted to the micropore size accessible to N_2 adsorbate [0,35-2 nm] – the mean values and distribution curves can be computed. Comparison with the micropore size distribution (PDF) calculated from the adsorption data is performed using effective spaces in the [0,35-2 nm] range. The pore size distribution was also evaluated using NLDFT approach. The best correspondence with results obtained by TEM and the calculations using the HK-model was achieved assuming mixed slit/cylinder shape of the pores (Fig. 4). This model is reasonable for polymer-derived ACs if the cylindrical shape is ascribed to the transport pores.

3.3. X-ray diffraction

Activated carbons may adsorb significant amounts of moisture from atmosphere. All adsorption properties are commonly exploited after vacuum annealing of the samples for different periods and similar procedures are often recommended to apply for characterization of ACs’ structure. Indeed, X-ray diffraction patterns of wet and dry samples of activated carbon may differ dramatically (Shiryaev et al., 2017). The sign and magnitude of the effect depend on the nature of electrostatic interaction of the adsorbate molecules with the graphitic crystallites: in some cases, the molecules between adjacent graphene stacks pull them together, leading to increased ordering, whereas in other cases (different surface chemistry of the AC and/or solvent) the solvent molecules penetrate into the stacks and thus decrease the crystallographic perfection.

Whereas it might seem that all structural characterizations should be performed on vacuum-annealed samples only, such approach also suffers from serious and poorly controlled complications. First, after the annealing the samples are usually analysed using X-rays and/or spectroscopic methods in air. Kinetics of the moisture adsorption, however, is almost never reported, although for materials with high specific surface it can be rather rapid (several minutes) as demonstrated by Infra-red absorption and photoluminescence study of

nanodiamond powder heated to various temperatures and cooled in air (Khomich et al., 2017). Moreover, the kinetics may vary widely for the ACs with different pore size distributions. Even high vacuum environment of a TEM column does not assure complete loss of the adsorbed moisture. For example, annealing of loose nanodiamond powder at 400 ºC in vacuum for few hours does not eliminate surface OH-groups completely (Maturilli et al., 2014). In addition, details of the porous structure and surface properties may be influenced by the temperature regime of the annealing. It is therefore extremely difficult to establish a robust procedure of the samples preparation, universally suitable for all ACs. In view of these complications, all X-ray and Raman measurements reported in this contribution were obtained on AC samples shelf-stored at identical conditions for comparable periods of time (at least 12 months), assuring attainment of "equilibrium" degree of moisture saturation, which, of course, is sample-dependent due to variations in pore sizes. For many samples, the measurements were repeated with intervals of several months and the diffraction patterns remained identical, thus validating consistency of the approach. Negligible effect of degassing on the structural features of carbon skeleton of several types of activated carbons was also noted in (Dmowski et al., 2011).

The X-ray diffraction patterns of all samples (Fig. 5a) are qualitatively similar and can be described by a model of crystallites of disordered graphitic carbon embedded into an amorphous carbon matrix. The sample-dependent variations in the 002 peak position, breadth and intensity are caused by distribution of sizes and crystallographic perfection of the graphene stacks. We have not attempted determination of the size of very small graphitic crystallites from X-ray diffraction due to ambiguity of the task: the result depends on the crystallite morphology and on several other parameters (Rutman and Skakov, 1989; Fujimoto, 2003). Analytical models describing Wide-angle X-ray scattering curves exist (e.g., Ruland and Smarsly, 2002; Puech et al., 2019), but they imply certain assumptions about the ordering of graphene sheets. Since the samples studied in our work were obtained from very different precursors, application of a single common model is barely justified. In addition, the proper modeling requires use of monochromatic incident radiation, whereas in our case only moderate monochromatisation by using K_β-filter was employed. This approach leads to certain broadening of the experimental profile due to contribution of $K_{\alpha 1}$ and $K_{\alpha 2}$ components (e.g., Puech et al., 2019).

XRD patterns are shown in Fig. 5. In Fig. 5a the samples are ordered from bottom to top according to volume of supermicropores, compare with Fig. 1. A general trend of

decreasing of the 002 peak relative intensity with increase of the porosity might be inferred, but the dependence is not uniform across the whole set of the ACs and strong variations are immediately observable and are explained by the precursor (see also Men'shikov et al., 2021). For example, the patterns of coal-derived BPL and BGX samples are very different despite similar values of $V_{supermicorpores}$. At the same time, for the FAS-type samples the intensity of the 002 reflection follows the porosity trend: the samples with the highest porosity – the polymer-derived FAS3 and FAS4 – possess very weak 002 reflection corresponding to a very small thickness of the ordered graphene stacks. Further support of very small thickness comes from symmetric profile of the peak at ~43° (an overlapping 10(0) and 101 reflections) (e.g., Puech et al., 2019). This observation is in line with TEM data, showing very small sizes of the ordered domains in those samples.

Despite consistent decrease of the 002 peak relative intensity, the 101 reflection corresponding to in-plane direction in the stacks does not follow same trend. This behavior can be explained by the development of the porosity in between the graphene sheets with a smaller amount of in-plane effects. The intensity ratio I(002)/I(10+101) as well as ratios of other reflections do not show clear correlation with other properties. The samples studied do not possess a clear 10 peak. Albeit the samples with the low surface area possess low intensity of the 002 reflection and small sizes of the crystallites as seen on 2D projections (TEM images), the correlation of the XRD data with the TEM results is less straightforward. The absence of a good quantitative correlation between these methods is explained by certain bias of the XRD towards larger crystallites giving rise to (broad) peaks, whereas the amorphous component, readily imaged in TEM, mostly contributes to the X-ray background.

Several samples with contrasting adsorption properties were studied using High-energy X-ray diffraction (Fig. 5c,d). Differences between the samples are subtle but for the samples with the highest porosity (e.g., FAS-type) the peak at 1.4 $Å^{-1}$ corresponding to neighboring C-atoms in a hexagon is broadened. The broadening may be interpreted in terms of defective rings (such as 5- and 7-member) or in terms of strained graphene sheets. The presence of carbon penta- or heptagons induces curvature of the sheetConsequently, separation of the pure strain contribution from that of defective hexagons is barely possible for a highly disordered material. Note, however, that in many cases such defected rings are adjacent; in such configurations the deviations from planarity are very small (Leyssale and Vignoles, 2014). Investigations using aberration-corrected HRTEM indeed showed presence of such rings in non-graphitising carbons (Guo et al., 2012, Allen et al., 2022). The pair

distribution function becomes strongly sample-dependent at distances >11 Å with considerable differences from high-quality graphite. This behavior reflects strong disorder along the c-axis of graphitic carbon (e.g., Dmowski et al., 2012). Oscillations of the RDF functions for the GF40 and BGX samples are less intense, indicating presence of a noticeable fraction of atoms heavier than carbon. Indeed, these samples contain appreciable amount of oxygen and nitrogen as shown by preliminary chemical analysis.

3.5. SAXS patterns

3.5.1. Data analysis

In discussion of the experimental SAXS patterns, we employ several parameters, see scheme in Fig 6a. The "slope" corresponds to power law dependence of the scattering by the pores, Guinier radius – R_G, which reflects the size (cross-section) of the pores and $I_{plateau}$ - the intensity of the plateau on the curve. The later parameter ($I_{plateau}$) is proportional to the relative fraction of defects, responsible for corresponding part of the SAXS curve, in this case to the fraction of the supermicropores. The slope and the $I_{plateau}$ may depend on the amount of adsorbed moisture and of other volatiles filling the pores, but experiments performed on several samples at temperatures between 25 and 100 °C in vacuum show lack of noticeable changes.

Our approach in interpretation of the SAXS curves from porous carbons is somewhat non-traditional, albeit less ambiguous (see Shiryaev et al., 2017). It is often assumed that the pore walls can be approximated by atomically flat surfaces with sharp change in the electronic density contrast. The scattering from an object with well-defined boundary should obey the Porod law with $Log(I) \sim q^{-4}$. Since SAXS patterns of porous carbons often deviate from this dependence, the deviation is forcibly removed by subtraction of a suitable background intensity, leading to the q^{-4} behaviour. Subsequently, the volume of the pores is calculated. The differences between the SAXS and adsorption data are then ascribed to a closed porosity. The assumption of the perfectly flat pore walls is largely inherited from a paper reporting investigation of carbonaceous fibers (Fourdeux et al., 1969). In those materials, indeed, the walls could be "atomically flat" as was shown by TEM imaging. The same assumption also appears to be correct for a number of other systems, for instance, for silica-based porous materials (e.g., Ruland and Smarsly, 2002). However, in many cases, the flat wall approximation is an oversimplification (see Pre et al., 2013; this work) and the "forced" background subtraction is then unphysical. The deviations from the Porod law can be explained by the existence of electron density gradients and fluctuations (Ruland, 1971). The

scattering curves from a system of pores with rough walls were calculated by direct modeling (Shiryaev et al., 2017). Therefore, we believe that an analysis of the SAXS curves from ACs should consider the "slope" parameter as a proxy of the electron density gradient, fluctuations or roughness of the pore wall.

3.5.2. SAXS results

SAXS patterns of the studied samples comprise two main regions corresponding to the scattering by macroscopic heterogeneities and by the pores (Fig. 6a). The major fraction of the total scattering intensity is due to the large heterogeneities with sizes exceeding the resolution of the employed setup (~65 nm). The Guinier plot ($\log(I)$-q^2) for the low q region is either not linear, or the linearity range is short, indicating that the large scatterers do not represent a monodisperse system. These heterogeneities could be tentatively assigned to graphitic crystallites or to macropores; their role in the sorption processes is minor. The scattering from these heterogeneities dominates at scales above 9-10 nm.

Three main groups of the samples, differing in degree of contribution of the pores into the scattering curve, can be distinguished. Fig. 6a shows typical curves for every group: the FAS4 represents a clear hierarchical system with strong contribution of the pores (this group includes TMC, FAS2, FAS3, FAS4, BPL, NC100); the samples FAS1 and MUST also show well-developed porosity, but the "plateau" is less pronounced reflecting relatively broad size distribution of pores; finally, the MUST900 sample shows only a weakly pronounced pores-related shoulder. The BGX sample possibly contains two populations of the heterogeneities.

The $I_{plateau}$ is anticorrelated with the ultramicroporosity fraction extracted from the adsorption data for most samples except the purely ultramicroporous TMC sample and for some highly activated furfural-derived ACs (Fig. 6b,c). The intensity of small-angle scattering is proportional to the product of the volume (V) and the electron density contrast $(\Delta\rho)^2$ of the scatterers and matrix. The observed negative correlation suggests that the ultramicropores are much weaker scatterers than the supermicropores (see also Shiryaev et al., 2017).

Considering only the values of the SAXS curves "slope", one may conclude that the TMC sample contains slit-like pores with sharp interfaces, since the "slope" is equal to an ideal value of -2 for disk-like objects (Fig. 6b). All other ACs show some gradient of electronic density. The spatial extension of the gradient is the largest for the BGX sample (the "slope" is -3.2), although this explanation is not unique.

Guinier radii (R_G) of the pores were calculated both in assumption of isometric (spherical) and slit-like pores. A linear correlation between the R_G and the mean micropore size is observed for the materials exhibiting similar fringe geometries in TEM images. Earlier (Shiryaev et al., 2017; Men'shchikov et al., 2020, 2021), we have shown that for the given set of ACs possessing similar structure, the R_G values correlate linearly with the pore widths extracted from N_2 adsorption data, but with an offset, see Fig. 6e,f. The offset is most likely caused by markedly different assumptions on pore-matrix interface structure employed in the calculation of these parameters, but exact reasons remain to be understood.

Somewhat unexpected and perhaps partly coincidental, a negative correlation is observed between the BSU% and R_G, i.e. between relative surface of the ordered graphene stacks observed in TEM and size of the pores evaluated from SAXS (Fig. 6g). Namely, for most samples except TMC, SC, and BGX, the BSU% decreases with increasing R_G. As discussed above, the TEM images indicate that the three "irregular" samples are characterized by the presence of large ordered assemblages and the pores are mainly located between them. Consequently, the R_G mainly reflects distance between the ordered, but still quasi-parallel graphene stacks, and thus may not be directly correlated with the BSU%. The negative correlation between the pore sizes and the ordering of the material observed for other samples likely reflects sensitivity of SAXS to specific types of the pores; here, we recall that SAXS is mainly sensitive to the supermicropores.

3.6. Raman scattering

First order Raman spectra of sp^2 carbons consists of two main peaks – D and G (Ferrari and Robertson, 2001; Merlen et al., 2017) (Fig. 7a). However, several additional components are obvious in many cases and albeit their assignment is subject of long-standing debates, their inclusion into consideration significantly improves the fit of experimental spectra (e.g., Shiryaev et al., 2017; Merlen et al., 2017 and refs. therein), see Fig. 7a. A rather detailed computational study (Smith et al., 2016) assigns these spectral bands to specific defects in graphenes and their stacks. In our work, we have employed two independent approaches for decomposition of the first order Raman bands. The first one assumes a pseudo-Voigt shape of the peaks. Whereas it allows very good fitting of experimental spectra, it requires calculation of a Lorentzian/Gaussian ratio for every peak, thus considerably increasing number of free fitting parameters. The second approach fixes a Lorentzian for the

G-peak and Gaussian shapes for the D-band, the "amorphous" or the A-peak, and the trans-polyacetylenes (TPA) band (Fig. 7a). Both approaches for the decomposition gave similar results; below, we discuss values obtained using the second approach.

Figures 7b,c displays spectroscopic parameters of both G and A bands. For the G-peak an inverse (quasi)linear correlation is observed between the position of the G-peak maximum (σ_G) and its FWHM (Full Width and Half-Maximum) for the studied samples. For comparison, trends established for hydrogenated amorphous (a-C:H), tetrahedral hydrogenated and non-hydrogenated (ta-C:H and ta-C, respectively) amorphous carbons are also shown. In this coordinates the samples with less ordered structure display the lowest σ_G values; more ordered samples possess higher σ_G. The linear trends for the three types of activated carbons mentioned above tend to agglomerate around a point at $\Gamma_G \approx 50$ cm^{-1} and $\sigma_G \approx 1610$ cm^{-1}. The behavior of the G and A bands for the studied samples differ notably. The points for the G band are situated at the top of the trend for the a-C:H, representing a subset with narrow G-peaks; the G-peak positions correspond to a nanocrystalline graphite. The samples BGX and GF40 possibly share features typical for both a-C:H and ta-C:H carbons. It appears that the G-peak in our samples is dominated by relatively ordered graphitic crystallites, whereas less-ordered material is responsible for the broad Gaussian A-peak. Interestingly, examination of G peak FWHM values obtained from the spectra measured at different excitation energies indicate that the samples can be split into several groups (Fig. 7c): whereas the majority follows expected 1:1 trend, the coal- and furfural-derived materials form individual distinct sets.

Since the I_D/I_G is a (indirect) measure of defects' density and size of the continuous graphitic domains, a broad negative correlation between the intensity ratio surface of Bulk structural units as measured in TEM images is not surprising (Fig. 7e). Interestingly, the G peak systematically narrows with increasing density of the carbon skeleton (Fig. 7f).

Examination of the position and FWHM of the A-peak allows splitting the samples into two main groups. The first one comprises the majority of the studied ACs and is characterized by a somewhat larger FWHM (120-190 cm^{-1}) and A-peak positions between 1540–1560 cm^{-1}. The second group includes highly activated furfural-derived samples for which relatively small FWHM (70-110 cm^{-1}) and A-peak positions between 1510-1530 cm^{-1} are observed. The sample BPL falls approximately in between these groups and the sample BGX is characterized by an unusually large FWHM, but belongs to the same quasi-linear

trend on the FWHM-position line for the A-peak, i.e. to the first group. At close examination of the G-peak behavior, the samples from the second group also form a distinct set with slightly lower G-peak positions (~1590 cm^{-1}) and larger FWHM. It is not yet entirely clear why the particular set of the furfural-derived ACs form the separate group, but according to TEM and XRD these samples are very disordered with a small amount of ordered graphene stacks. These samples also possess high porosity and HEXRD suggests presence of defective carbon rings.

Comparison of Raman data with structural parameters extracted from TEM image processing is shown in Figs. 7e and 8. Figure 8a reveals that materials with markedly different values of fringe tortuosity form separate groups also when spectral parameters (D, G peaks positions and FWHM, intensity ratio) are considered. Although the trends are not systematic (with possible exception of the D peak position and the tortuosity for most of the samples), the grouping is rather obvious. The furfural-derived materials again form a separate group and the coal-derived BPL falls in between the FAS samples and the rest of the set.

Since the position of defects-related Raman peaks may shift with excitation wavelength, let us define the dispersion of the G band as: $[\sigma_G(\lambda_1) - \sigma_G(\lambda_2)]/[\lambda_1 - \lambda_2]$, where λ_1 = 785 nm and λ_2 = 532 nm. Figure 8b displays the evolution of the D band position (σ_D) recorded at 532 nm (upper part), and the dispersion of the G band (bottom part) as a function of length of the continuous graphene stacks, L_d, obtained from TEM image analysis. We recall here that the D-peak is related to the breathing modes of the aromatic rings. For a perfect graphite, σ_D measured using 532 nm excitation should be equal to 1340 cm^{-1}. Such values are observed for the ACs with L_d>0.8 nm. For the L_d less than 0.55 nm, the σ_D can reach higher values (1345 to 1355 cm^{-1}) implying influence of compressive stress on the breathing modes of the aromatic rings [Gouadec and Colomban, 2007]. For the L_d close to 0.6 nm, the σ_D can be as low as 1330 cm^{-1}, indicating influence of tensile stress. The qualitative change occurs for the L_d values between 0.5 and 0.6 nm, which roughly corresponds to a transition between two to three aromatic rings in size (Fig. 8b). The highest compressive stress is found for the GF40 sample, made by chemical activation of olive seeds. This sample is also characterized by significant negative dispersion of the D peak position.

One can see that the furfural-derived samples forming a separate group on σ_D - FWHM plot for the A-peak, also form a distinct cloud of points on both panels of the Figure 8. These samples are characterized by the small fringe length, the D-peak is

downshifted and is positively dispersed; the tensile stress is the most pronounced. A logical explanation of the peculiar behavior of these samples in the studied collection is that their precursor is a non-graphitising carbon, thus the carbonization and subsequent activation lead to formation of highly irregular pores. The SAXS data suggest presence of a large gradient of electronic density in the pores in these materials, which may be interpreted as a complex interface of the pore void and wall and thus existence of significant fraction of highly disordered sp^2-C. This explanation does not necessarily contradict the hypothesis about the influence of compressive stress on the D-peak behavior; it rather indicates that several factors can affect vibrational spectra of aromatic rings.

Another dense group on the Figure 8b is formed by pine-wood-derived MUST samples. These carbons were activated at various temperatures (750 and 850 °C) for different times. Nevertheless, from the point of view of Raman spectroscopy they form a rather compact group. For three of these samples, SAXS results suggest that the pores are decently approximated by slit-like morphology. In the sample with the smallest degree of activation the pores are closer to rod-like shape. TEM indicates large fraction of the BSU's and/or continuous domains and the gas adsorption suggests domination of the supermicropores. Presumably, the pores in these samples are located in between (quasi)parallel graphene stacks.

Raman data together with TEM and adsorption measurements point to an interesting correlation: the ACs with higher influence of the stretching (the furfural-derived FAS samples) are characterized by larger specific surface measured by N_2 adsorption. The A and TPA bands are the weakest in these materials. In addition, these samples are characterised by the largest total volume of ultra- and supermicropores and the smallest length of continuous domains (see Fig. 2d). Furthermore, the pores' surface as measured by BET method systematically increases with decrease of the IA/I_G ratio (Fig. 9). This behavior suggests that the A peak probes an amorphous phase; removal of this phase makes ultra- and supermicropores accessible to probing gases.

4. Conclusions

Structure and adsorption properties of activated carbons produced from markedly different precursors (coconut shell, pine wood, coals, furfural) are studied by complementary methods allowing access to various structural scales. The principal aim is to relate porosity with the structural peculiarities of the studied materials. Whereas it is impossible to propose a

single set of parameters showing general correlation for all samples, for a given set of activated carbons, most often obtained from a same precursor, common trends could be derived.

Processing of Transmission Electron Microscopy (TEM) images allows to classify the studied samples according to size and surface density of the «continuous domains», thus highlighting the degree of disorder of the activated carbons at nanoscale. The distribution of fringe lengths and the mean curvature radius of the graphene sheets also differ for the samples from the different groups.

Comparison of the TEM and Small-Angle X-ray scattering data with the micropore size data derived from gas adsorption isotherms suggest that the shape of the super-micropores (0.7-2 nm) strongly deviates from the ideal slit pore model. Presumably, this implies that these large pores are related to a random arrangement of the continuous domains and resulting mismatch voids. The shape of these pores may be thus highly variable.

X-ray diffraction patterns of the samples correspond to a model of disordered graphitic carbon crystallites embedded into an amorphous carbon matrix. The sample-dependent variations in the graphite 002 diffraction peak are caused by scatter in sizes and crystallographic perfection of the graphene stacks. A general trend of decreasing relative intensity of the 002 peak with increased porosity of a specimen is observed. The low intensity of this reflection in the highly porous samples corresponds to markedly decreased thickness of the ordered graphene stacks. This observation is in line with TEM images, showing very small sizes of the ordered domains in those samples.

Analysis of the Small-angle X-ray scattering patterns suggests that the ultramicropores are much weaker scatterers than supermicropores. For a given set of activated carbons possessing similar structure, the Guinier radii (R_G) linearly correlate with the pore widths extracted from the N_2 adsorption data, but with an offset. The offset is tentatively explained by differences in assumptions on pore-matrix interface structure employed in the calculations of these parameters, but exact reasons remain to be understood. Comparison with TEM image analysis suggests that for the supermicropores the R_G mainly reflects the distance between the ordered, quasi-parallel graphene stacks.

The Raman scattering data are not well correlated with results of other employed methods, most likely due to sensitivity of the Raman signal to atomic-scale level. However, combination of the spectroscopic data with TEM and adsorption may suggest that the activated carbons with higher influence of stretching of the graphene sheets are characterized

by larger specific surface as measured by N_2 adsorption. The A peak observed in Raman spectra corresponds to an amorphous phase, which clogs ultra- and supermicropores.

Statements and Declarations: The authors declare absence of conflict of interests

Acknowledgements. We highly appreciate important contribution of Dr. A. Shkolin in discussion of NLDFT data. Comments of two anonymous reviewers helped to improve the paper.

REFERENCES

Allen, C.S., Ghamouss, F, Boujibar, O., Harris, P.J.F.: Aberration-corrected transmission electron microscopy of a non-graphitizing carbon, Proc Roy Soc A, 578 20210580 (2022).

Atkinson, D., McLeod, A.I., Sing, K.S.W.: Adsorptive properties of microporous carbons: primary and secondary micropore filling. J. Chim. Phys., 81, 791-794 (1984).

Dmowski, W., Contescu, C.I., Llobet, A., Gallego, N.G., Egami, T.: Local Atomic Density of Microporous Carbons, J. Phys. Chem. C, 116, 2946–2951 (2012)

Dubinin, M.M.: The Potential Theory of Adsorption of Gases and Vapors for Adsorbents with Energetically Nonuniform Surfaces. Chem. Rev., 60(2), 235–241 (1960)

Dubinin, M.M.: Physical adsorption of gases and vapors in micropores. In: Cadenhead, D. A. (ed.) Progress in surface and membrane science, 9. pp. 1–70, Academic Press, New York (1975)

Dubinin, M.M.: Fundamentals of the theory of adsorption in carbon adsorbents: characteristics of their adsorption properties and microporous structures. Carbon, 27, 457–467 (1989)

Fourdeux, A., Herinckx, C., Perret, R., Ruland, W.: La structure des fibres de carbone. C.R. Acad. Sci. Paris C, 269, 1597-1600 (1969)

Ferrari, A.C., Robertson, J.: Resonant Raman spectroscopy of disordered, amorphous, and diamond-like carbon. Phys.Rev. B, 64, 075414 (2001)

Fujimoto, H.: Theoretical X-ray scattering intensity of carbons with turbostratic stacking and AB stacking structures. Carbon, 41, 1585–1592 (2003)

Gouadec, G., Colomban, P.: Raman spectroscopy of nanomaterials: How spectra relate to disorder, particle size and mechanical properties. Prog. Cryst. Growth Charact. Mater. 53, 1–56 (2007)

Gregg, S. J., Sing, K.S.W: Adsorption, surface area and porosity. Academic Press, London (1982)

Guo, J., Morris, J.R., Ihm, Y., Contescu, C.I., Gallego, N.C., Duscher, G., Pennycook, S.J., Chisholm, M.F.: Topological Defects: Origin of Nanopores and Enhanced Adsorption Performance in Nanoporous Carbon, Small, 8(21), 3283–3288 (2012)

Jagiello, J., Olivier, J.P.: A Simple Two-Dimensional NLDFT Model of Gas Adsorption in Finite Carbon Pores. Application to Pore Structure Analysis. J.Phys. Chem. C 113(45), 19382-19385 (2009)

Khomich, A.A., Kudryavtsev, O.S., Dolenko, T.A., Shiryaev, A.A., Fisenko, A.V., Konov, V.I., Vlasov, I.I.: Anomalous enhancement of nanodiamond luminescence on heating. Laser Physics Letters 14(2), 025702, DOI: 10.1088/1612-202X/aa52f5 (2017)

Kratky, O.: Instrumentation. Experimental technique, slit collimation. In: Glatter, O., Kratky O. (ed.) Small angle X-ray scattering, Ch. 3.I. pp. 53–84, Academic Press, New York (1982)

Lake, J.A.: An iterative method of slit-correcting small-angle X-ray data. Acta. Cryst., 23, 191-194 (1967)

Leyssale, J.-M., Da Costa, J.-P., Germain, C., Weisbecker, P., Vignoles, G.L.: Structural features of pyrocarbon atomistic models constructed from transmission electron microscopy images. Carbon, 50, 4388–4400 (2012)

Leyssale, J.M. and Vignoles, G.L. :: A large-scale molecular dynamics study of the divacancy defect in graphene. J. Phys. Chem. C, 118(15), 8200–8216 (2014)

Maturilli, A., Shiryaev, A.A., Kulakova, I.I., Helbert, J: Infra-Red Reflectance and Emissivity Spectra of Nanodiamonds, Spectroscopy Letters, 47(6), 446-450 (2014)

Men'shchikov, I. E., Shkolin, A., Strizhenov, E., Khozina, E., Chugaev, S., Shiryaev, A., Fomkin, A., Zherdev, A.: Thermodynamic Behaviors of Adsorbed Methane Storage Systems Based on Nanoporous Carbon Adsorbents Prepared from Coconut Shells. Nanomaterials, 10, 2243; doi:10.3390/nano10112243 (2020)

Men'shchikov, I.E., Shiryaev, A.A., Shkolin, A.V., Visotskii, V.V., Khozina, E.V., Fomkin, A.A.: Carbon adsorbents for methane storage: genesis, synthesis, porosity, adsorption. Korean Journal of Chemical Engineering, 38(2), 276-291 (2021)

Merlen, A., Buijnsters, J.G., Pardanaud, C.: A Guide to and Review of the Use of Multiwavelength Raman Spectroscopy for Characterizing Defective Aromatic Carbon Solids: from Graphene to Amorphous Carbons. Coatings, 7, 153; doi:10.3390/coatings7100153 (2017)

Pardanaud, C., Giacometti, G., Martin, C., Ruffe, R., Angot, T., Aréou, E., Pégourié, B., Tsitrone, E., Dittmar, T., Hopf, C., Jacob, W., Schwarz-Selinger, T., Roubin, P.: Raman study of CFC tiles extracted from the toroidal pump limiter of Tore Supra. J. Nucl. Mat., 415(1), S254-S257 (2011).

Pardanaud, C., Martin, C., Roubin, P.: Multiwavelength Raman spectroscopy analysis of a large sampling ofdisordered carbons extracted from the Tore Supra tokamak. Vibrational Spectroscopy, 70, 187–192 (2014)

Pré, P., Huchet, G., Jeulin, D., Rouzaud, J.N., Sennour, M., Thorel, A.: A new approach to characterize the nanostructure of activated carbons from mathematical morphology applied to high resolution transmission electron microscopy. Carbon, 52, 239-258 (2013).

Puech, P., Dabrowska, A., Ratel-Ramond, N., Vignoles, G.L., Monthioux, M. : New insight on carbonisation and graphitisation mechanisms as obtained from a bottom-up analytical approach of X-ray diffraction patterns. Carbon, 147 602-611 (2019).

Ruland, W.: Small-angle scattering of two-phase systems: determination and significance of systematic deviations from Porod's law. J Appl Cryst., 4, 70-73 (1971)

Ruland, W., Smarsly, B.: X-ray scattering of non-graphitic carbons: an improved method of evaluation. J Appl Cryst., 35, 624–633 (2002)

Rutman, A.M., Skakov, Yu.A.: Radial distribution functions of atoms and interference functions of partly ordered carbon materials. I. Influence of edge atoms of disperse layers. Sov. Phys. Cryst., 34(3), 338–341 (1989)

Quirico, E., Orthous-Daunay, F.-R., Beck, P. Bonal, L. Brunetto, R. Dartois, E., Pino, T., Montagnac, G., Rouzaud, J.-N., Engrand, C., Duprat, J.: Origin of insoluble organic matter in type 1 and 2 chondrites: New clues, new questions. Geochim. Cosmochim. Acta, 136, 80-99 (2014)

Shiryaev, A.A., Voloshchuk, A.M., Volkov, V.V., Averin, A.A., Artamonova, S.D.: Nanoporous active carbons at ambient conditions: a comparative study using X-ray scattering

and diffraction, Raman spectroscopy and N_2 adsorption, Journal of Physics: Conf. Series, 848, 012009 (20 pages) (2017) doi: 10.1088/1742-6596/848/1/012009

Smith, M.W., Dallmeyer, I., Johnson, T.J, Brauer, C.S, McEwen, J.-S., Espinale, J.F., and Garcia-Perez, M.: Structural analysis of char by Raman spectroscopy: Improving band assignments through computational calculations from first principles. Carbon, 100, 678–692 (2016)

Tsivadze, A.Yu, Gur'yanov, V.V and Petukhova, G.A.: Preparation of spherical activated carbon from furfural, its properties and prospective applications in medicine and the national economy. Prot. Metals and Phys. Chem. Surf. 47(5), 612–620 (2011)

Ustinov, E.A., Do, D.D.: Application of Density Functional Theory to analysis of energetic heterogeneity and pore size distribution of activated carbons, Langmuir 20, 3791–3797 (2004)

Vartapetian, R.Sh, Khozina, E.V.: Structure of rigid and swelling adsorbents according to pulsed NMR data on the mobility of adsorbed water and benzene molecules, Colloid J., 68(1), 1–19 (2006)

Table 1. Studied activated carbons

Sample	Precursor	Activation mode
BGX	Pine wood	Chemical, H_3PO_4
BPL	Bituminous coal	Physical, steam
GF40	Olive stones	Chemical, H_3PO_4
FAS (4 samples)	Furfural	Physical, steam
MUST (4 samples)	Pine	Physical, steam
NC-100	Coconut shell	Physical - steam
TMC	Bituminous coal	Physical, steam; hydrocarbon treatment

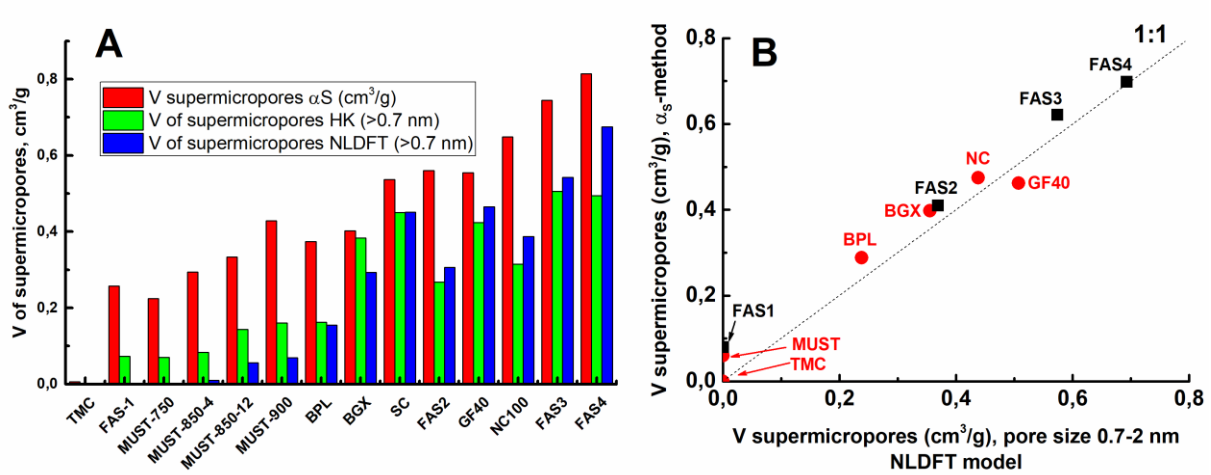

Fig 1. Results of adsorption measurements: volumes of micropores and of supermicropores as given by αS and NLDFT approaches. The furfural-derived FAS-type samples are marked by black squares, all other samples are shown as red disks.

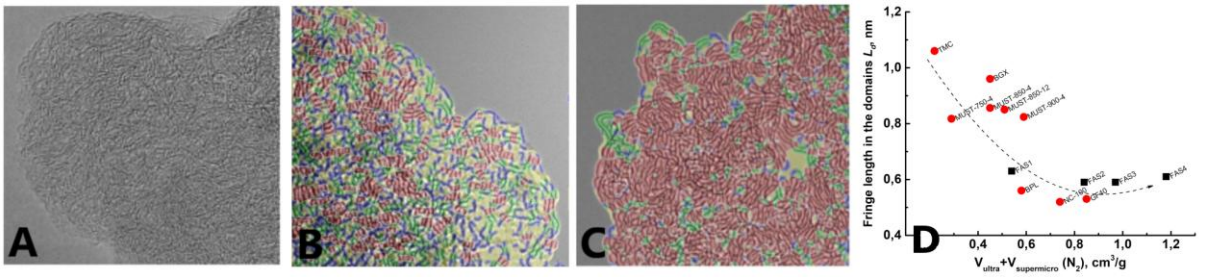

Fig. 2. Raw and processed Transmission Electron Microscopy images of active carbons with different degrees of the structural perfection (for the processing algorithm see Pre et al., 2013). A – Raw image of the FAS1, B – processed image of a highly disordered AC (BPL), C – processed image of an ordered AC (SC). Color legend for B, C: red - continuous domains formed by multiple stacked fringes, blue - single fringes; green - pairs of parallel fringe fragments; yellow - carbon free spaces. D – Total volume of ultra- and supermicropores as a function of fringe length in continuous domains. The furfural-derived samples (FAS) are marked as black squares, all other materials are shown as red circles. The dashed curve is just to guide an eye.

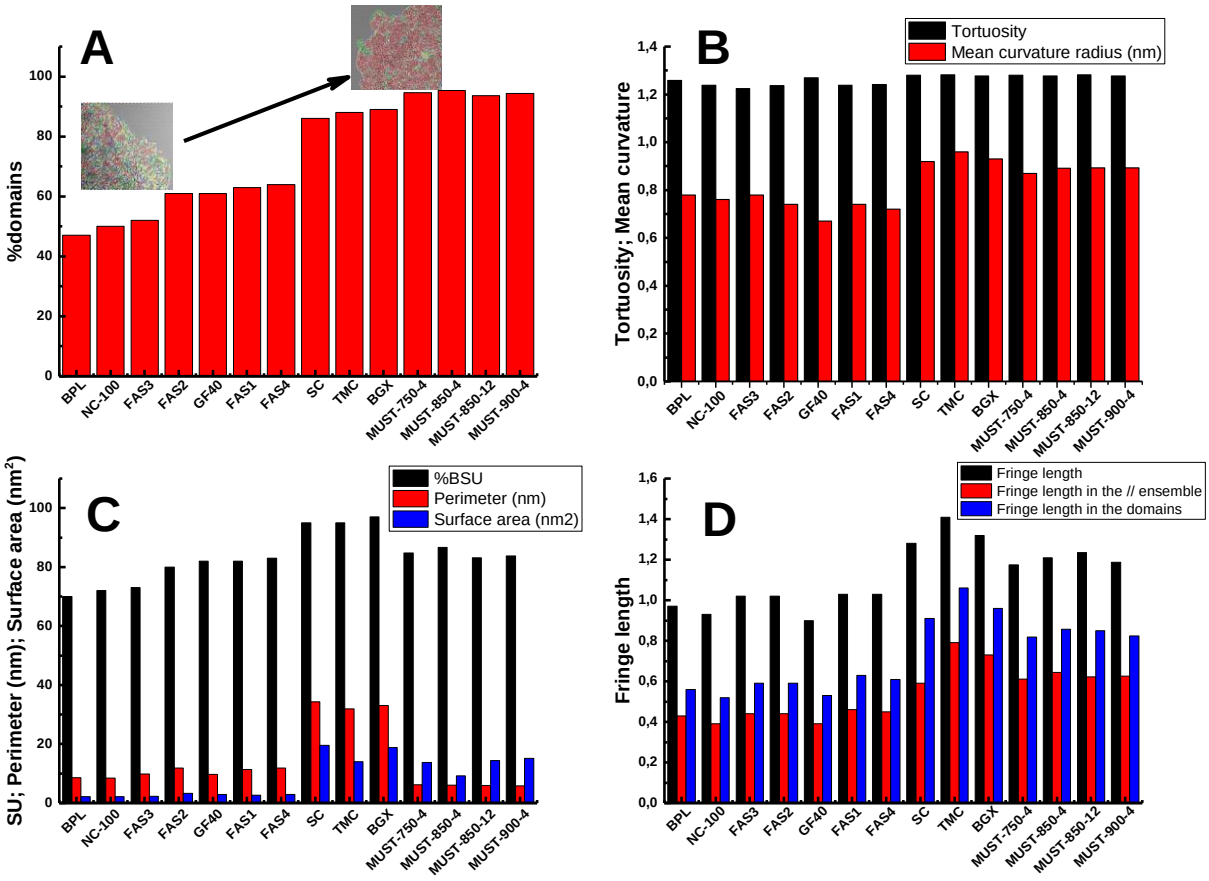

Fig. 3. Parameters obtained from TEM images processing. Inset in A shows processed TEM images highlighting differences in the structure (see text and Fig. 2).

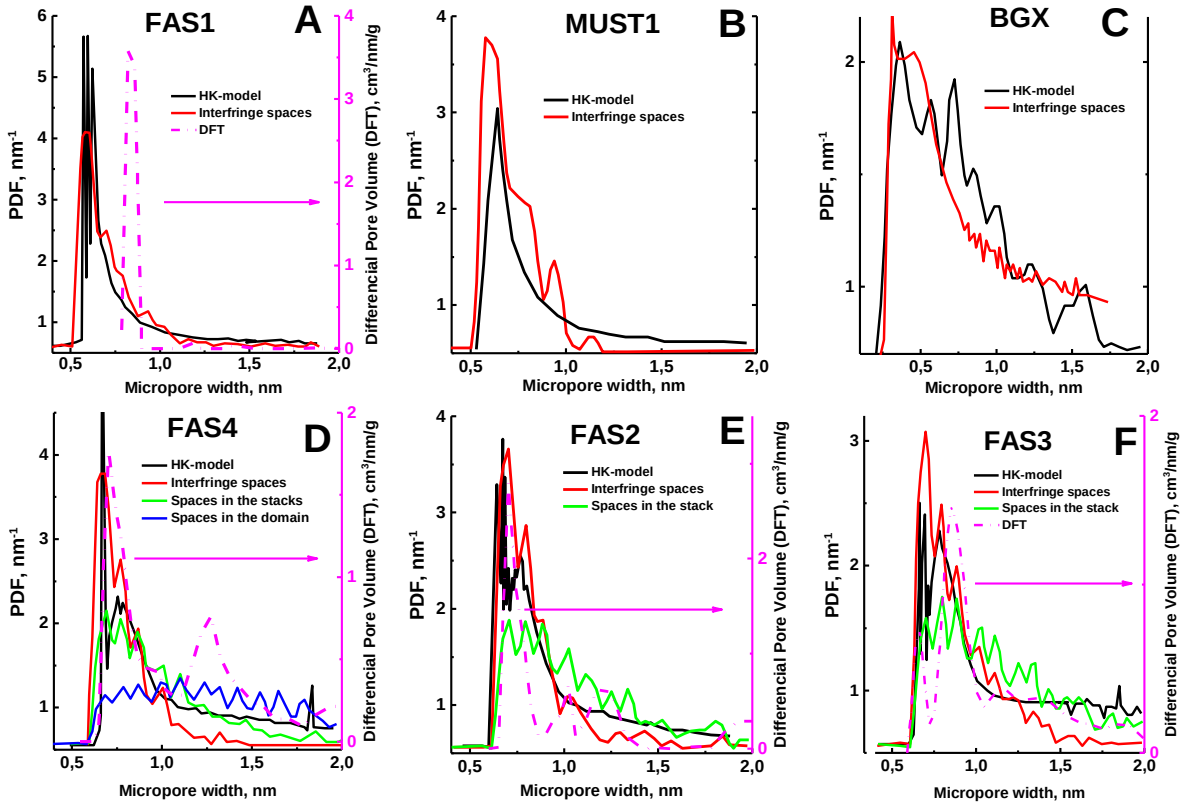

Fig. 4. Micropore size distributions (PDF) determined from the Horvath-Kawazoe (HK) model with the PDFs of the effective spaces measured in the different types of graphene stacks observed in TEM. For the FAS-type carbons results of NLDFT calculations are also shown; a mixed slit/cylinder model is assumed.

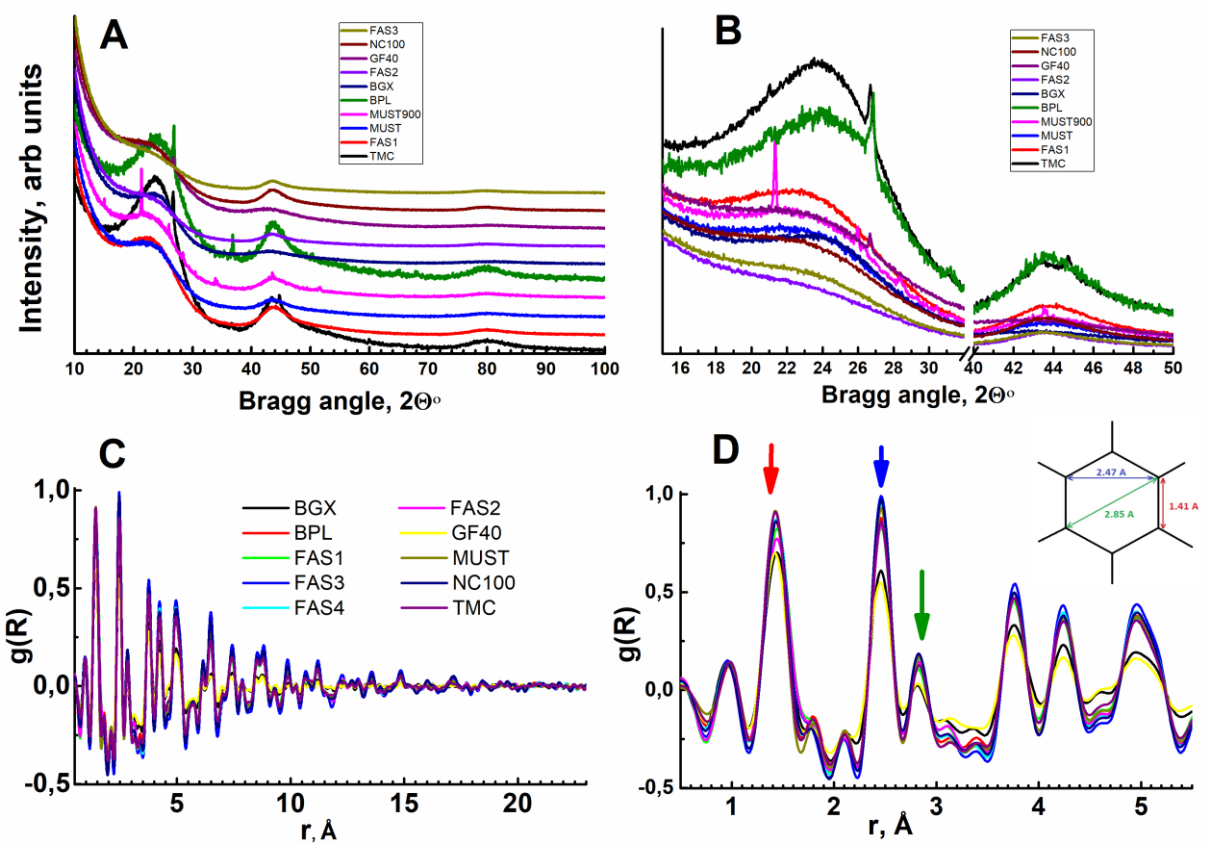

Fig. 5. X-ray diffraction patterns. A, B – conventional powder diffraction; the order of the curves corresponds to volume of supermicropores in the samples (see Fig. 1). In A the curves are normalised and displaced vertically for clarity. In B – zoomed region comprising the most prominent 002 and overlapping 10(0) + 101 reflections ; note a break of the horizontal axis. C, D – High energy XRD, overall view (C) and a zoomed region (D). Inset in D shows scheme of a carbon hexagon with the principal interatomic distances.

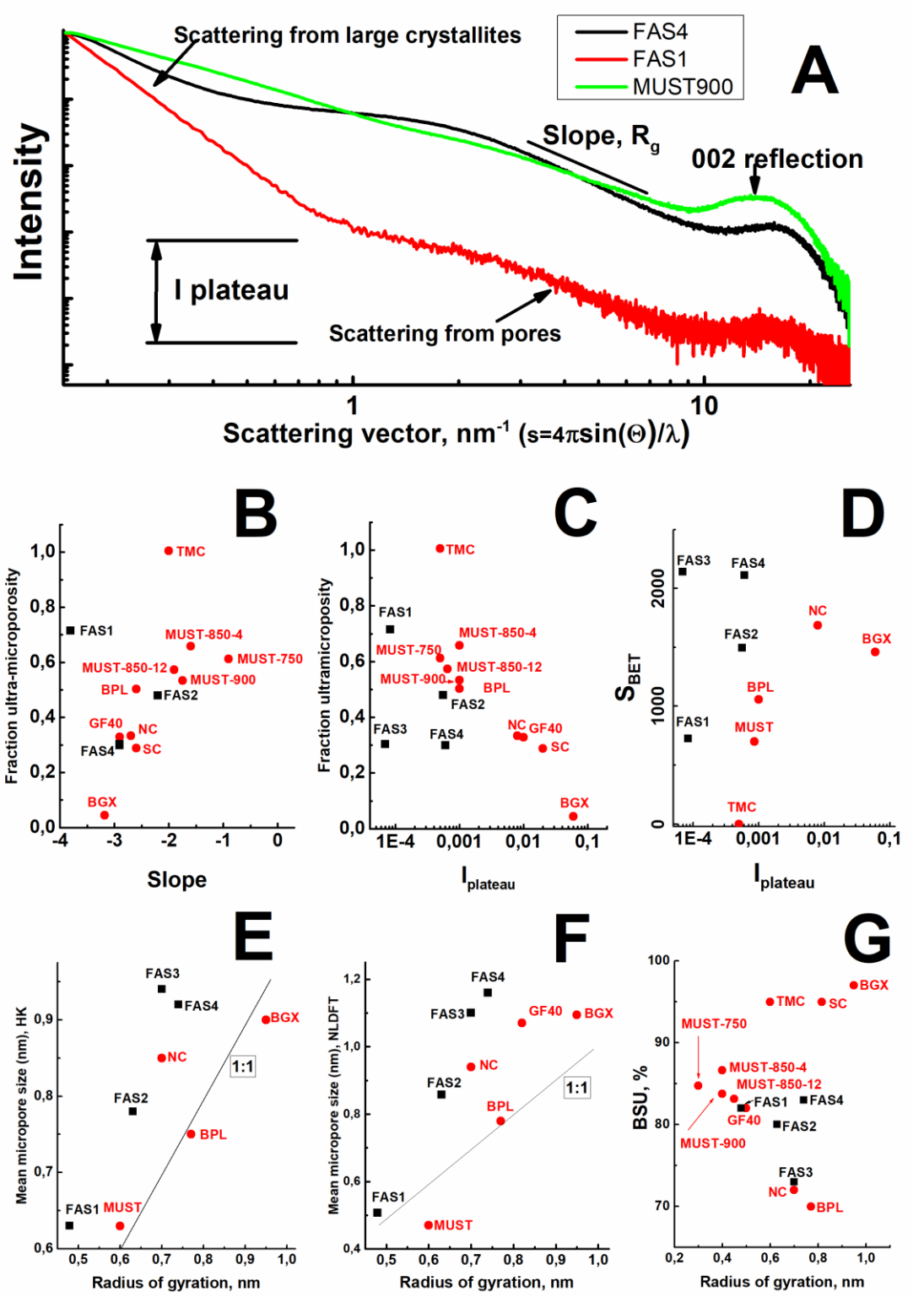

Fig. 6. Small-angle X-ray scattering. A – general view of the scattering curves for three representative samples and notations of analysed parameters. B-F – scatter plots of the parameters derived from the SAXS curves and from the adsorption data. G – correspondance of the gyration radius (or Guinier) and BSU fraction obtained from the TEM images processing. The furfural-derived FAS-type samples are marked by black squares, all other samples are shown as red circles.

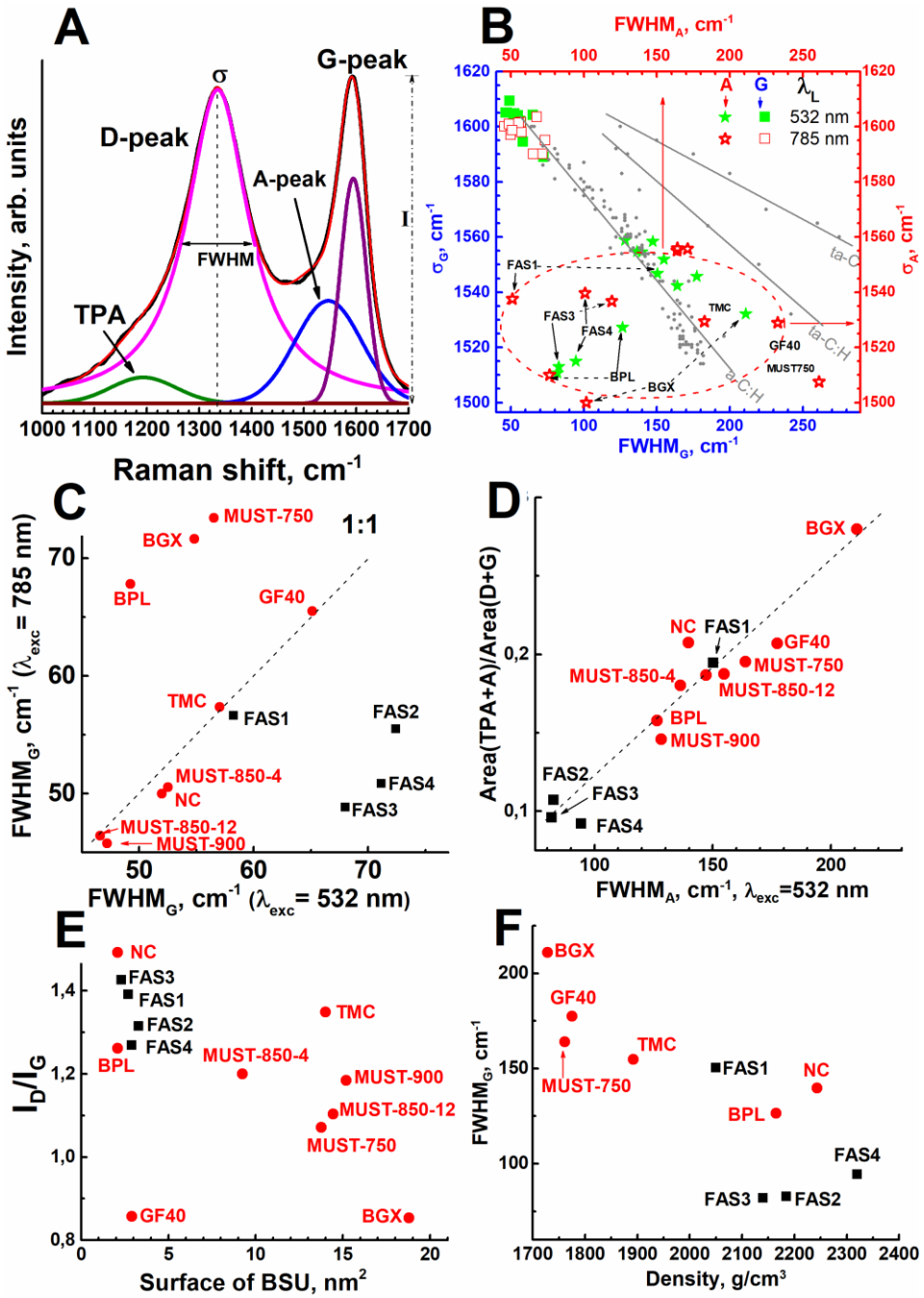

Fig. 7. Raman spectroscopy. A – An example of decomposition of the one-phonon region with notations used in the data treatment. B – positions and FWHM values of the G (left and bottom axes) and A (right and top axes) peaks of the studied samples as recorded at different excitation wavelengths. Small dots show values for the G-peak from: Ferrari and Robertson, (2001), Pardanaud et al., (2011, 2014), Quirico et al., (2014). C – Correlation between FWHM values of the G peak as measured at different excitation wavelengths; the dashed line shows 1:1 ratio. D – Relationship of total area (A + TPA-related peaks) and FWHM of the A peak. The dashed line is to guide an eye. E – Intensity ratio of the D to G peaks as a function of surface of bulk structural units observed in TEM images. F – correlation between width of the G peak and density as measured by He picnometry. The furfural-derived FAS-type samples are marked by black squares, all other samples are shown as red circles.

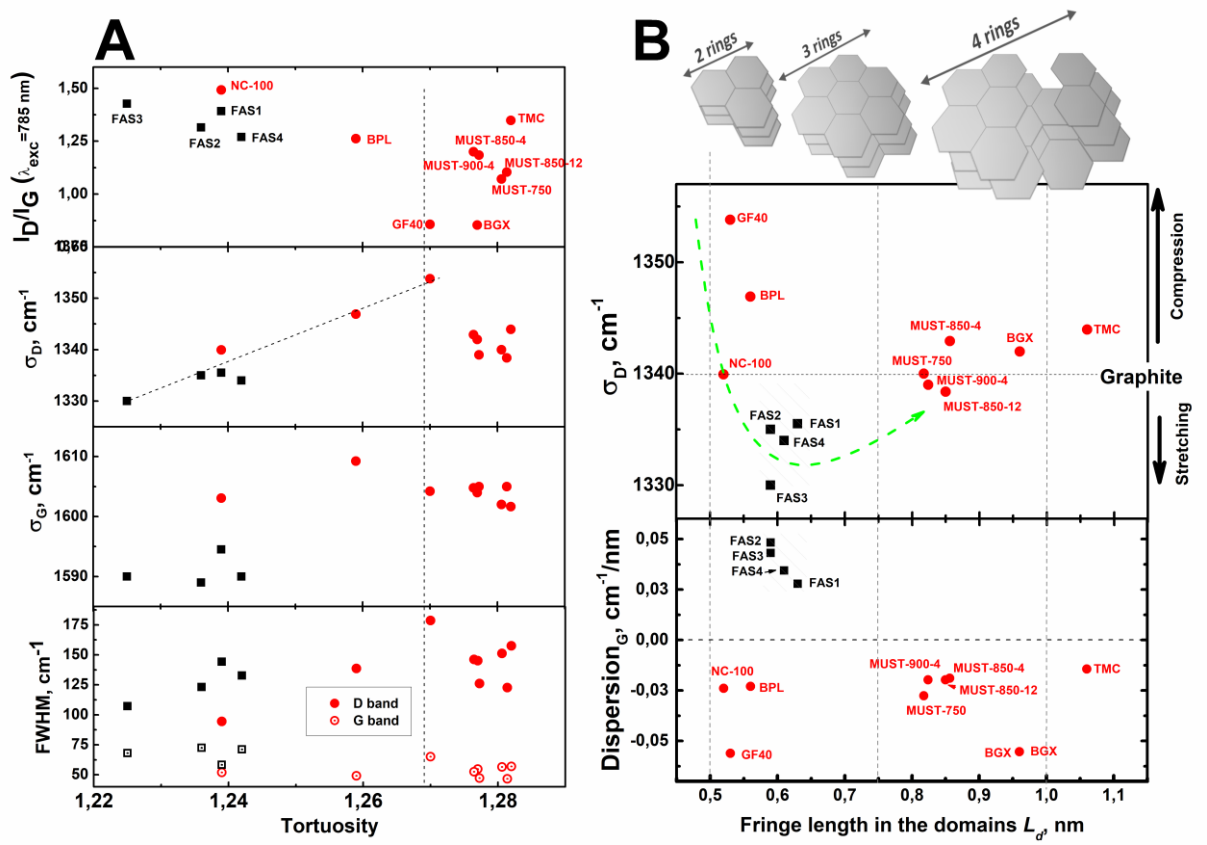

Fig. 8. Correlations between parameters of the Raman peaks and of structural characteristics derived from TEM image processing. The furfural-derived FAS-type samples are marked by black squares, all other samples are shown as red circles. Dashed vertical line and arrow are to guide an eye.

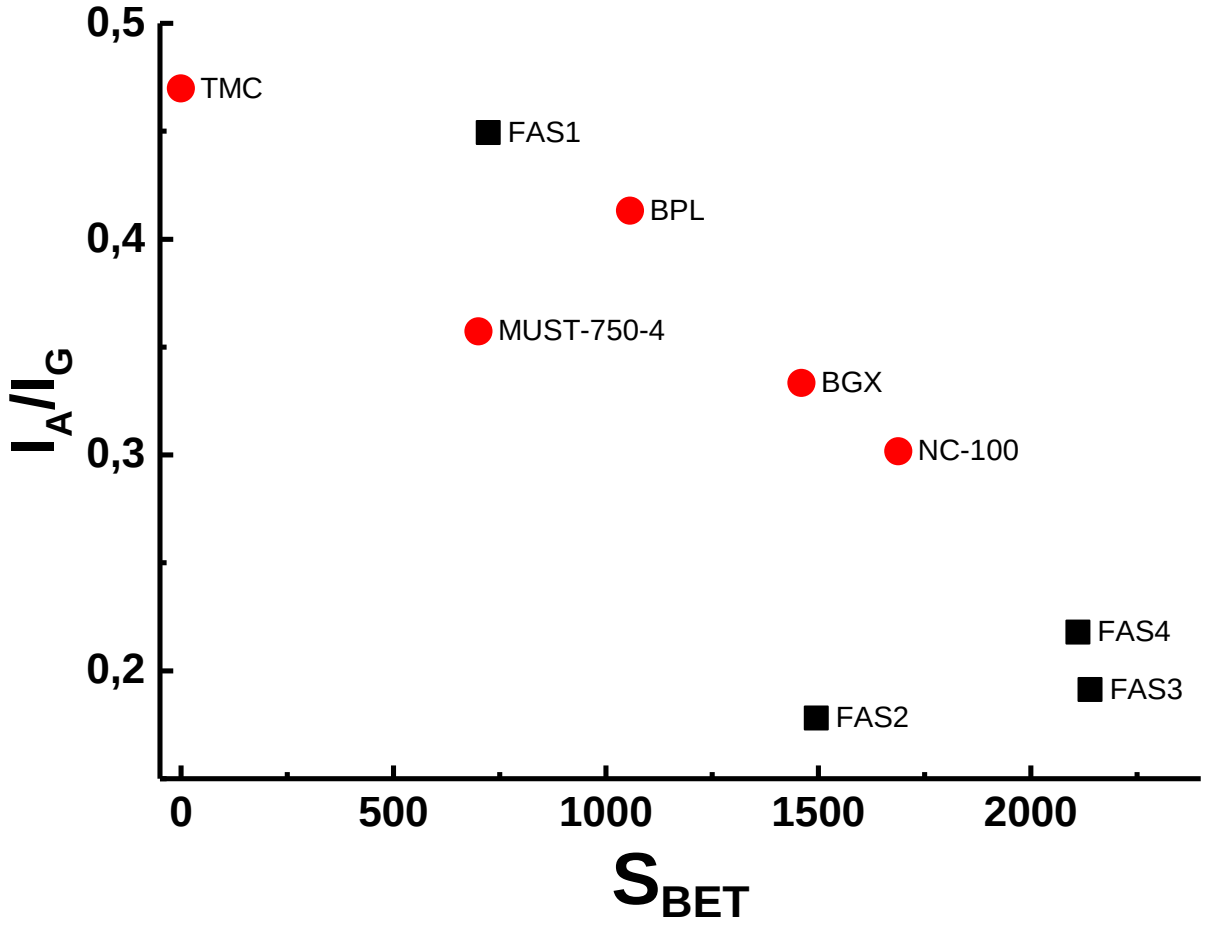

Fig. 9. Correlation between Raman spectroscopy and adsorption measurements. The furfural-derived FAS-type samples are marked by black squares, all other samples are shown as red circles.